





# High-velocity outflows persist up to 1 Gyr after a starburst in recently quenched galaxies at $z > 1$

Elizabeth Taylor <sup>1</sup>★, David Maltby,<sup>1</sup> Omar Almaini <sup>1</sup>, Michael Merrifield <sup>1</sup>, Vivienne Wild <sup>2</sup>,  
Kate Rowlands <sup>3</sup> and Jimi Harrold <sup>1</sup>

<sup>1</sup>*School of Physics and Astronomy, University of Nottingham, Nottingham NG7 2RD, UK*

<sup>2</sup>*School of Physics and Astronomy, University of St Andrews, North Haugh, St Andrews KY16 9SS, UK*

<sup>3</sup>*Department of Physics and Astronomy, Johns Hopkins University, Baltimore, MD 21218, USA*

Accepted 2024 October 28. Received 2024 October 15; in original form 2024 July 8

## ABSTRACT

High-velocity outflows are ubiquitous in star-forming galaxies at cosmic noon, but are not as common in passive galaxies at the same epoch. Using optical spectra of galaxies selected from the UKIDSS Ultra Deep Survey at  $z > 1$ , we perform a stacking analysis to investigate the transition in outflow properties along a quenching time sequence. To do this, we use Mg II ( $\lambda 2800 \text{ \AA}$ ) absorption profiles to investigate outflow properties as a function of time since the last major burst of star formation ( $t_{\text{burst}}$ ). We find evidence for high-velocity outflows in the star-forming progenitor population ( $v_{\text{out}} \sim 1400 \pm 210 \text{ km s}^{-1}$ ), for recently quenched galaxies with  $t_{\text{burst}} < 0.6 \text{ Gyr}$  ( $v_{\text{out}} \sim 990 \pm 250 \text{ km s}^{-1}$ ), and for older quenched galaxies with  $0.6 < t_{\text{burst}} < 1 \text{ Gyr}$  ( $v_{\text{out}} \sim 1400 \pm 220 \text{ km s}^{-1}$ ). The oldest galaxies ( $t_{\text{burst}} > 1 \text{ Gyr}$ ) show no evidence for significant outflows. Our samples show no signs of active galactic nucleus (AGN) in optical observations, suggesting that any AGN in these galaxies have very short duty cycles, and were ‘off’ when observed. The presence of significant outflows in the older quenched galaxies ( $t_{\text{burst}} > 0.6 \text{ Gyr}$ ) is difficult to explain with starburst activity, however, and may indicate energy input from episodic AGN activity as the starburst fades.

**Key words:** galaxies: evolution – galaxies: formation – galaxies: high-redshift – galaxies: ISM.

## 1 INTRODUCTION

The evolution of galaxies from blue, gas-rich and disc-like objects to red, compact and passive structures is a well-studied area of astrophysics, yet many key puzzles remain unsolved. One such puzzle is how and why galaxies have their star formation activity ‘quenched’. Star formation peaked in the most massive galaxies during the epoch commonly referred to as ‘cosmic noon’ – from  $z \sim 3$  to  $z \sim 1$  – which makes it the ideal period to catch galaxies in the process of quenching (see e.g. Ilbert et al. 2013; Muzzin et al. 2013; Papovich et al. 2018; Leja et al. 2020; Santini et al. 2022; Taylor et al. 2023; Weaver et al. 2023). Different quenching mechanisms are expected to act on different time-scales, leading to varying spectral features and morphological properties in the quenched systems.

An important mechanism used in models and simulations of quenching is feedback, both from stellar activity and active galactic nuclei (AGNs; see Heckman & Best 2014; Veilleux et al. 2020, and references therein). Massive bursts of star formation supply large amounts of energy from supernova ejecta and radiation, which can generate outflowing galactic-scale winds detectable out to the virial radii of galaxies (e.g. Murray, Ménard & Thompson 2011; Borthakur et al. 2013). Furthermore, high levels of star formation activity are thought to fuel ‘radiative-mode’ AGNs, which can also produce

winds capable of rapidly quenching a galaxy (Veilleux et al. 2020). The outflows from stellar and AGN processes can eject or heat the cold gas reservoirs required for further star formation, potentially leading to a decline in the overall star formation rate (SFR), and an eventual evolution of a galaxy on to the red sequence. In addition, it has been suggested that feedback from ‘jet-mode’ AGNs may be required to prevent any further gas cooling and inhibit rejuvenation (e.g. Cielo et al. 2018; Kondapally et al. 2023).

High-velocity outflows are ubiquitous in star-forming galaxies (SFGs) at cosmic noon, both with and without AGNs (e.g. Hainline et al. 2011; Bradshaw et al. 2013; Cimatti et al. 2013; Bordoloi et al. 2014; Talia et al. 2017), but are uncommon in old quiescent galaxies at the same epoch (e.g. Maltby et al. 2019). Recent work has found evidence that outflow velocity depends on various properties, such as SFR and SFR–density (e.g. Heckman et al. 2015; Heckman & Borthakur 2016), and (more weakly) on stellar mass (Davis et al. 2023), suggesting that star formation may be the root of galactic-scale winds.

One population ideal for studying how outflows affect galaxy evolution are recently quenched – also referred to as post-starburst (PSB) – galaxies (see Wild et al. 2016; Rowlands et al. 2018; French 2021). PSBs are galaxies that have undergone a recent and rapid quenching event after a heightened period of star formation, and are easily identified by the unique shape of the resulting spectral energy distributions (SEDs; e.g. Wild et al. 2014; Park et al. 2023). Spectroscopically, they show strong Balmer absorption lines typical

\* E-mail: [elizabeth.taylor@nottingham.ac.uk](mailto:elizabeth.taylor@nottingham.ac.uk)

of young A and F stars, and absent nebular emission lines (Dressler & Gunn 1983). At  $z \sim 0.6$ ,  $\sim 1000 \text{ km s}^{-1}$  outflows have been detected in the most luminous PSBs, with debate over whether the winds originate from highly compact starbursts (Diamond-Stanic et al. 2012; Sell et al. 2014; Perrotta et al. 2021) or from AGN feedback (Tremonti, Moustakas & Diamond-Stanic 2007). Nevertheless, these outflows may represent the residual signature of a feedback event which quenched the galaxy.

At higher redshift, studies have found similar results. Maltby et al. (2019) found similarly high-velocity outflows ( $v_{\text{out}} \sim 1150 \text{ km s}^{-1}$ ) in a sample of 40 PSBs at  $z > 1$  which showed no AGN signatures in their optical data. They conclude that these PSBs were either quenched solely by stellar feedback from an intense episode of star formation, or that any AGN episode which may have contributed to the winds has now faded. Conversely, Man et al. (2021) detected  $\sim 1500 \text{ km s}^{-1}$  outflows in two gravitationally lensed recently quenched galaxies at  $z \sim 3$  with emission line ratios that could indicate AGN activity (see also Belli et al. 2023). Similarly, Davies et al. (2024) found 14 objects in their sample of star-forming and quenching galaxies ( $1.7 < z < 3.5$ ) with neutral gas outflows they attribute to AGN feedback.

Recently, some work has been done to investigate how outflows evolve alongside their host galaxy in the local Universe; Sun et al. (2024) found outflow velocities decreasing with time since a starburst in a sample of 80 000 galaxies using SDSS. However, until now, no such study has been undertaken at high redshift. In this work, we use high-redshift ( $z \geq 1$ ) PSBs and recently quenched galaxies within the Ultra Deep Survey (UDS; PI: Almaini) field, along with highly star-forming and passive galaxies, to determine how outflow velocity varies with time since a starburst.

The structure of this paper is as follows: In Section 2, we present our data, sample selection, and stacking procedure. In Section 3, we outline our methods and results, and discuss these further in Section 4. We end with our conclusions and a brief summary in Section 5. Throughout this paper, we adopt the AB magnitude system and a flat  $\Lambda$ CDM cosmology with  $\Omega_{\text{M}} = 0.3$ ,  $\Omega_{\Lambda} = 0.7$ , and  $H_0 = 100h \text{ km s}^{-1} \text{ Mpc}^{-1}$  where  $h = 0.7$ .

## 2 DATA

### 2.1 The UDS: photometry and spectroscopy

The UDS is the deepest near-infrared survey conducted over  $\sim 0.8 \text{ deg}^2$ , and the deepest component of the United Kingdom Infrared Telescope (UKIRT) Infrared Deep Sky Survey (UKIDSS; Lawrence et al. 2007). We use the UDS Data Release 11 (DR11) catalogue, which reaches a  $5\sigma$  limiting depth of  $J = 25.6$ ,  $H = 25.1$ , and  $K = 25.3$  in 2-arcsec diameter apertures. Further details can be found in Almaini et al. (2017) and Wilkinson et al. (2021). Full details of the DR11 catalogue will be presented in Almaini et al. (in preparation).

The UDS imaging is complemented by additional deep photometric data in nine other bands:  $B$ ,  $V$ ,  $R$ ,  $i'$ , and  $z'$ -band optical observations from the Subaru *XMM-Newton* Deep Survey (SXDS; Furusawa et al. 2008),  $U'$ -band photometry from the CFHT Megacam, mid-infrared photometry ( $3.6 \mu\text{m}$  and  $4.5 \mu\text{m}$ ) from the *Spitzer* UDS Legacy Program (SpUDS, PI: Dunlop), and deep  $Y$ -band data from the VISTA VIDEO survey (Jarvis et al. 2013). The area of the UDS covered by all 12 bands is  $0.62 \text{ deg}^2$ . The resulting 12-band photometry is used to derive photometric redshifts for all galaxies in the survey, which form the basis for subsequent galaxy classifications (Section 2.1.1) and pre-selection for follow-up spectroscopy (Section 2.1.2). Further details of the photometric

redshift determination can be found in Wilkinson et al. (2021). In this work, we also make use of  $K$ -band structural parameters from Almaini et al. (2017).

#### 2.1.1 Galaxy properties and classification

To separate SFGs, passive galaxies, and PSBs, we use the principal component analysis (PCA) technique established by Wild et al. (2014, 2016). In brief, the aim of the PCA method is to describe the broad range of galaxy SEDs using the linear combination of a small number of components. It is found that three components are needed to sufficiently account for the variance in SEDs, with the amplitude of each component being termed a ‘supercolour’ (SC1, SC2, and SC3). The first two supercolours are utilized in this work, where SC1 and SC2 correlate with mean stellar age and stellar mass build-up within the last Gyr, respectively. Galaxies can be classified based on their position in an SC1–SC2 diagram, where the population boundaries are determined by comparison to model SEDs and spectroscopy. We note that, while dust and age are degenerate with SC1 alone, SC2 and SC3 help to break this degeneracy and allow us to separate dusty SFGs from older passive systems. For a more detailed explanation of the supercolour analysis, see Wild et al. (2014).

In this work, we use the photometric SC galaxy classifications to split our sample. For PSB galaxies, photometric classification is arguably more reliable than spectroscopy alone (see Wild et al. 2020), since it samples a much wider portion of the SED. Galaxy properties used in this work (e.g. stellar mass, burst mass fraction, time since burst) are derived from the fitting of several 10 000’s of Bruzual & Charlot (2003) stellar population models to the first three supercolours, with the precise number of models depending on the redshift of the galaxy. These ‘stochastic burst’ models are the same as those used in Kauffmann et al. (2003), and are formed from exponentially declining SFRs with random  $\delta$ -function bursts with varying strengths and ages superposed. They have a range of formation times, exponential decay times, metallicity, and dust contents. Galaxy properties are then estimated from the median of the posterior probability distribution in the usual way. For full details of the method, see Kauffmann et al. (2003). Of particular importance in this work are the burst mass fraction ( $f_{\text{burst}}$ ) and time since burst ( $t_{\text{burst}}$ ) properties. Burst mass fractions are calculated as the fraction of stellar mass formed in bursts in the past Gyr compared to the total stellar mass. The  $t_{\text{burst}}$  values provide the lookback time to the last burst in the galaxy star formation history. The supercolour technique was originally established using the UDS DR8 catalogue (Wild et al. 2014), and in this work we use the analysis applied to the full DR11 catalogue (see Wilkinson et al. 2021).

#### 2.1.2 Spectroscopy

The UDS contains  $\sim 8000$  sources with deep optical spectroscopy – assembled from several programmes which target a large range of galaxy type – from star-forming to passive. The UDSz is the spectroscopic component of the UDS, where spectra were obtained for over 3000  $K$ -band selected galaxies using both the VIMOS and FORS2 instruments on the ESO VLT, as part of the UDSz ESO Large Programme (180.A-0776, PI: Almaini).<sup>1</sup> In this work, we utilize the UDSz-FORS2 (McLure et al. 2013) spectra, which have spectral resolutions of  $R \sim 660$  and exposure times of 5.5 h. The VIMOS instrument was used by Maltby et al. (2016) for

<sup>1</sup><https://pleiades.nottingham.ac.uk/ppadm1/UDSz>

spectroscopic follow-up of an additional  $\sim 100$  photometrically selected PSB galaxies identified in Wild et al. (2014) (UDSz-VIMOS+, 094.A.0410, PI: Almaini), to confirm the validity of their PCA (see Section 2.1.1). For the ancillary UDSz-VIMOS+, the observations have  $R \sim 580$  and an exposure time of 4 h. The UDS field is also targeted by the VANDELS spectroscopic survey (ESO programme 194.A-2003, McLure et al. 2018; Garilli et al. 2021), which provides spectra with exposure times of 20 or 40 h, and a resolution of  $R \sim 580$ . Spectroscopic redshifts ( $z_{\text{spec}}$ ) are determined from these data sets using a cross-correlation of spectral templates via the EZ package (Garilli et al. 2010). In this work, we use spectra with secure redshifts for  $z_{\text{spec}} \geq 1$ , which results in a parent sample of 1045 objects – of objects with SC classes, 375 are star-forming (SFG), 196 are quiescent (referred to as PAS), and 41 are PSBs.

## 2.2 Sample selection

In this work, we analyse the structure of the Mg II ( $\lambda\lambda 2796, 2803 \text{ \AA}$ ) absorption profile, which is a sensitive tracer of the low ionization interstellar medium (ISM). Blueshifted components in this profile are indicative of ISM outflows. To investigate the evolution of the Mg II absorption feature we select galaxies from our parent sample using the following criteria:

(i) Full wavelength coverage of the Mg II and [O II] features ( $2700 \text{ \AA} \leq \lambda \leq 3800 \text{ \AA}$ ) for SFGs, plus additional coverage of the Ca II H & K lines for PAS and PSB ( $2700 \leq \lambda \leq 4000 \text{ \AA}$ ). This is to ensure that  $z_{\text{spec}}$  for the input galaxies is determined using a spectral feature *other* than Mg II.

(ii) A signal to noise over the Mg II feature of  $S/N_{\text{Mg II}} > 1$ . This removes the influence of poor quality spectra on our stacks.

After checking to ensure redshifts were determined from stellar absorption features and/or bright emission lines via visual inspection, we find 264 objects matching these criteria (117 SFGs, 111 PAS, and 25 PSBs). We then further split our sample into four groups, to represent a likely evolutionary sequence for rapidly quenched galaxies. For our first group, we select SFGs we consider ‘progenitors’, using the boundaries  $SC2 > 4$  and  $SC2 \geq 0.25 \times SC1$ . We choose these boundaries based on the evolutionary tracks from Wild et al. (2016); we expect most galaxies in this region are likely progenitors for galaxies that will soon quench after forming a large fraction (10 per cent or greater) of their mass recently. This is further confirmed using statistical modelling based on simulated galaxy properties obtained using semi-analytical models (Harold et al., in preparation). We then select two recently and rapidly quenched populations of passive galaxies and PSBs, split by time since their most recent starburst: Quenched<sub>young</sub> ( $t_{\text{burst}} < 0.6 \text{ Gyr}$ ) and Quenched<sub>mid</sub> ( $0.6 < t_{\text{burst}} < 1 \text{ Gyr}$ ). To ensure that our progenitors and quenched samples are likely to follow the same evolutionary pathway, we apply a cut on the fraction of mass that has been built up in the past 1 Gyr, of 10 per cent or greater ( $f_{\text{burst}} > 0.1$ ), to the Quenched<sub>young</sub> and Quenched<sub>mid</sub> samples. This criterion removes 23 SC passive (PAS) galaxies from the Quenched<sub>mid</sub> sample, although we note that repeating our analysis with no cut on  $f_{\text{burst}}$  has no significant impact on our results. When stacking the 23 removed galaxies alone, we find no evidence for an outflow. Our final group contains passive and PSB galaxies with  $t_{\text{burst}} > 1 \text{ Gyr}$ , hereafter Quenched<sub>old</sub>. By design, our Quenched<sub>old</sub> has no  $f_{\text{burst}}$  cut applied, as these galaxies are selected to have quenched more than 1 Gyr ago. The  $t_{\text{burst}}$  values used to split the samples are based on the stochastic burst models (see Section 2.1.1), although we note that time-scales

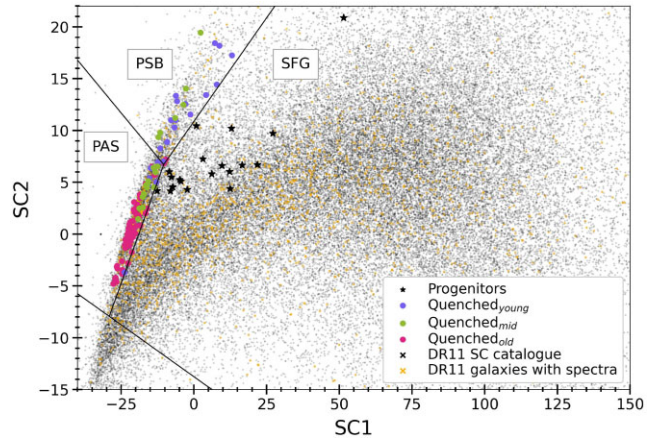


**Figure 1.** SC1–SC2 diagram showing the locations of the different groups within our sample. The four groups (Progenitors, Quenched<sub>young</sub>, Quenched<sub>mid</sub>, and Quenched<sub>old</sub>) represent a time sequence since the last starburst. SC1 and SC2 correlate with mean stellar age and stellar mass build-up within the last Gyr, respectively.

determined from alternative methods do not appear to affect our conclusions (see Section 4.2 for further discussion). The locations of the members of each group within the SC1–SC2 diagram are shown in Fig. 1. Final sample numbers and median values for the properties of each group are shown in Table 1.

## 2.3 Stacking procedure

To effectively identify any outflow signatures, we undertake a stacking analysis to increase the effective S/N across the Mg II absorption feature. We shift all individual input spectra to their rest-frame wavelengths using their spectroscopic redshifts (see Section 2.1). The spectra are resampled on to the same wavelength axis ( $\Delta\lambda = 0.25 \text{ \AA}$ ), preserving the integrated flux, and the entire spectrum is normalized for the total flux over  $2700 \text{ \AA} \leq \lambda \leq 2900 \text{ \AA}$  with the Mg II and Mg I ( $\lambda 2852 \text{ \AA}$ ) profiles masked out. The spectra are combined to create a median stack, after which we perform a  $3\sigma$  clip to minimize the effect of noise: we remove any input spectra where more than 10 per cent of flux points over  $2700 \text{ \AA} \leq \lambda \leq 2900 \text{ \AA}$  lie  $3\sigma$  or more away from the median stack. All remaining spectra are then combined to generate a single, final median stack. The effective spectral resolutions of the stacks are  $\Delta\lambda_{\text{FWHM}} \sim 5.4$  and  $\sim 5.6 \text{ \AA}$  for our progenitors and quenched samples, respectively. Uncertainties in the stack are the mean of the standard error from 100 bootstrapped simulated stacks. The resulting composite spectra are shown in Fig. 2. The stacks have been smoothed using a Gaussian filter with  $\sigma = 1.5 \text{ \AA}$  for display purposes only – this  $\sigma$  value was chosen as it is below the effective resolution of our stacks ( $\sigma_{\text{stack}} \sim 2.4 \text{ \AA}$ ). Equivalent width measurements for the Mg II, [O II], and H $\delta$  features, and the D4000 index for each group are shown in Table 2; the median values for each sample and the values as measured from the stacks are included, and show the expected behaviour with time since burst. The equivalent width values are measured using integration, using the wavelength ranges in Table 2.

## 3 ANALYSIS

A visual inspection of our four Mg II profiles shows clear asymmetry in all but the Quenched<sub>old</sub> sample ( $t_{\text{burst}} > 1 \text{ Gyr}$ ), which has a much broader, but symmetric, profile. The ratio of the sum of

**Table 1.** Final sample numbers and properties of our galaxy groups. The four groups represent a time sequence since the last starburst. For our quenched (Quenched<sub>y</sub>) groups, the numbers shown in brackets are those for passive galaxies and PSBs, respectively. The last section of the table shows median values for each property.

	Progenitors	Quenched <sub>young</sub>	Quenched <sub>mid</sub>	Quenched <sub>old</sub>
Time since burst (Gyr)	–	$\leq 0.6$	0.6–1	$\geq 1$
Classification	SFGs	PAS/PSB	PAS/PSB	PAS/PSB
Other criteria	Location in SC space	$f_{\text{burst}} \geq 0.1$		–
$N_{\text{spectra}}$	19	21 (6, 15)	21 (15, 6)	59 (57, 2)
—UDSz-FORS2	11	4 (0, 4)	6 (3, 3)	20 (21, 1)
—UDSz-VIMOS +	2	5 (1, 4)	1 (1, 0)	5 (4, 1)
—VANDELS	6	12 (5, 7)	14 (11, 3)	34 (36, 0)
Median values				
$\log_{10}(M_*/M_{\odot})$	10.31	10.77	10.81	11.02
$z_{\text{spec}}$	1.43	1.27	1.32	1.26
$t_{\text{burst}}$ (Gyr)	–	0.58	0.76	1.19
$K_{\text{AB}}$	21.98	20.69	20.99	20.49
$r_e$ (kpc; $K_{\text{band}}$ )	1.71	1.26	1.24	2.39
$n$ ( $K_{\text{band}}$ )	1.84	2.95	3.30	3.26

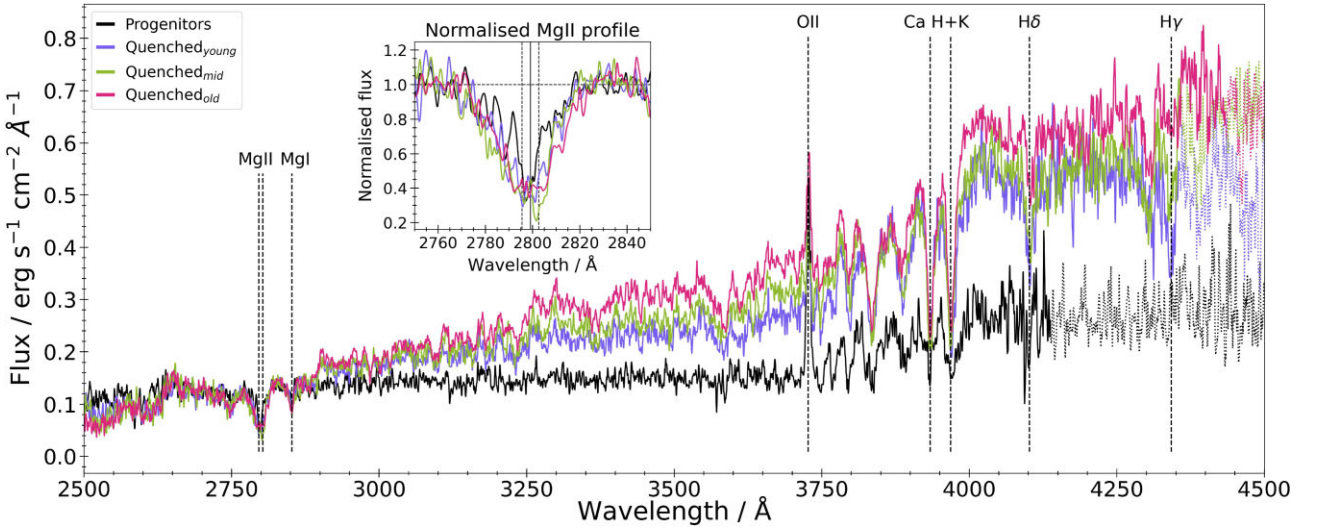


**Figure 2.** Median stacks for each group in our sample. Key spectral features are labelled. The stacks have been smoothed using a Gaussian filter with width  $\sigma = 1.5 \text{ \AA}$  for display purposes only. The dotted portion of each stack represents the wavelengths at which less than 50 per cent of input spectra have coverage. The Mg II absorption feature is shown in more detail in the sub-panel, and has been continuum normalized to allow for comparison between stacks. The dashed vertical lines in the inset denote the Mg II  $\lambda\lambda 2796, 2803 \text{ \AA}$  lines. The solid vertical line denotes the Mg II centroid at  $2799.1 \text{ \AA}$ .

**Table 2.** Equivalent width measurements of key spectral features for each group, calculated using integration. Columns (2)–(4) show the wavelength ranges used to calculate the equivalent widths. The ‘median’ column for each group is the median value of measurements from the individual input spectra. The ‘stack’ column for each group is the value as measured from the stack (shown in Fig. 2).

	Blue continuum ( $\text{\AA}$ )	Line ( $\text{\AA}$ )	Red continuum ( $\text{\AA}$ )	Progenitors		Quenched <sub>young</sub>		Quenched <sub>mid</sub>		Quenched <sub>old</sub>	
				Median	Stack	Median	Stack	Median	Stack	Median	Stack
$W_{\text{Mg II}} (\text{\AA})$	2762–2782	2784–2814	2818–2838	7.7	$7.8 \pm 1.3$	11.9	$12.2 \pm 0.9$	14.5	$13.4 \pm 1.9$	12.4	$13.3 \pm 0.7$
$W_{[\text{O III}]} (\text{\AA})$	3653–3713	3713–3741	3741–3801	–26.4	$-17.5 \pm 3.2$	–2.5	$-2.0 \pm 1.4$	–0.8	$-0.9 \pm 0.8$	–3.7	$-4.4 \pm 1.0$
D4000	3750–3950	–	4050–4250	1.53	$1.5 \pm 0.1$	1.56	$1.7 \pm 0.1$	1.67	$1.7 \pm 0.04$	1.77	$1.8 \pm 0.04$
$W_{\text{H}\delta} (\text{\AA})$	4030–4082	4082–4122	4122–4170	3.6	$2.8 \pm 1.2$	5.2	$5.4 \pm 0.9$	4.2	$4.6 \pm 1.2$	1.8	$2.2 \pm 0.7$

the fluxes either side of the Mg II centroid reveals a significant excess of blueshifted absorption ( $\sim 14$  per cent) in our first three groups, implying these galaxies harbour galactic-scale outflows. In Quenched<sub>old</sub>, this excess is only  $\sim 5$  per cent.

In this section, we outline two methods of measuring the outflow velocity,  $v_{\text{out}}$ , in each sample. We start with a simple double Gaussian model (Section 3.1), decomposing the Mg II absorption feature into separate systemic and outflowing ISM absorption components. In the

**Table 3.** F-test  $p$ -values and velocity measurements for each method, where  $\Delta v$  is the velocity offset measured from our fits, and  $v_{\text{out}}$  is the calibrated outflow velocity, as determined from our simulations. The significance of the outflowing component for each method is evaluated using an F-test, which produces a  $p$ -value – the necessity of an outflowing component is rejected if  $p_F > 0.05$ . Outflows are detected in the progenitor, Quenched<sub>young</sub> and Quenched<sub>mid</sub> samples, as seen from the  $p_F$  values. Outflows are not detected in the Quenched<sub>old</sub> sample, and hence we use ‘–’ for this column.

	Progenitors	Quenched <sub>young</sub> $t_{\text{burst}} < 0.6$ Gyr	Quenched <sub>mid</sub> $0.6$ Gyr $< t_{\text{burst}} < 1$ Gyr	Quenched <sub>old</sub> $t_{\text{burst}} > 1$ Gyr
Double Gaussian model				
F-test for outflow ( $p_F$ )	0.035	0.023	0.0059	0.53
$\Delta v$ (km s <sup>-1</sup> )	1850 ± 130	1690 ± 260	1790 ± 130	–
$v_{\text{out}}$ (corrected, km s <sup>-1</sup> )	1510 ± 140	1350 ± 260	1450 ± 140	–
Double Gaussian + stellar model				
F-test for outflow ( $p_F$ )	0.017	0.021	0.0046	0.39
$\Delta v$ (km s <sup>-1</sup> )	1740 ± 200	1330 ± 250	1730 ± 220	–
$v_{\text{out}}$ (corrected, km s <sup>-1</sup> )	1400 ± 210	990 ± 250	1390 ± 220	–
Boxcar				
$\langle v_{\text{out}} \rangle$ (km s <sup>-1</sup> )	730 ± 110	680 ± 80	760 ± 80	–

second method, we also include an initial subtraction of the stellar continuum via spectral fitting (Section 3.2). The significance of the outflowing component for each method is evaluated using an F-test, which produces a  $p$ -value – the necessity of an outflowing component is rejected if  $p > 0.05$ . The  $p$ -values and velocity values for each method are presented in Table 3. The uncertainties for all methods are determined by repeating the relevant procedure on 100 simulated spectra generated via a bootstrap analysis. The resulting fits to our absorption profiles presented here are smoothed as described in Section 2.3, for display purposes only. All analysis is performed on the non-smoothed stacks. We compare the benefits and drawbacks of each model in Section 4.1.

### 3.1 Double Gaussian model

In order to determine the significance of the asymmetry of our Mg II profiles, and to isolate any outflowing gas, we first use a double Gaussian decomposition model. Following the approach of Maltby et al. (2019), the model is fit using the following procedure:

(i) The continuum flux either side of the Mg II profile (2750 Å  $\leq \lambda \leq$  2850 Å) is normalized, using a smoothing spline fit.

(ii) Due to the lower resolution of our input spectra, the Mg II doublet ( $\lambda\lambda$ 2796, 2803 Å) is unresolved in our stacks, so we first need to estimate the spectral broadening of the absorption feature. To do this, a single Gaussian doublet ( $G_{\text{initial}}$ ) is fit to the Mg II profile, with the centroids fixed at the rest-frame wavelengths for systemic absorption. The doublet intensity ratio is set as 1.2:1, as seen for high- $z$  galaxies in Weiner et al. (2009). We note that using a doublet intensity ratio of 2:1, corresponding to the optically thin limit (see e.g. Steidel & Sargent 1992), has no significant impact on our results. To avoid any potential contamination of the broadening estimate by outflowing gas, we fit  $G_{\text{initial}}$  to the red side of the absorption feature only ( $\lambda \geq$  2803 Å).

(iii) We then fit the Mg II profile with a two-component model, using two Gaussian doublets. The first component ( $G_{\text{sys}}$ ) models the systemic absorption (stellar + ISM) and the second component ( $G_{\text{out}}$ ) models the outflow. The centroid of  $G_{\text{sys}}$  is fixed at the rest-frame wavelength, while the amplitude is allowed to vary. The centroid and amplitude of  $G_{\text{out}}$  are left free. The width of both doublets is fixed at the value determined by  $G_{\text{initial}}$ . Comparison of the centroids of the two components provides a wavelength offset,  $\Delta\lambda$ , which can be used to estimate the velocity offset of the outflowing gas,  $\Delta v$ .

For each group, 100 simulated median stacks are generated via a bootstrap analysis, and the fitting routine is repeated on each stack. The uncertainty in  $\Delta\lambda$  is the  $1\sigma$  error of the resulting 100 velocity measurements.

We then perform a calibration of our velocity offsets ( $\Delta v$ ) to estimate the typical outflow velocity,  $v_{\text{out}}$  of each of our samples. To do this, we follow the procedure presented in Maltby et al. (2019).<sup>2</sup> We simulate 2000 Mg II profiles exhibiting a range of outflow velocities, with random noise generated to match the typical S/N of our real galaxy spectra. We then generate a median stack of these profiles, and fit the double Gaussian model as described above. We find our model fits recover velocity offsets,  $\Delta v$ , that are systematically  $\sim 340$  km s<sup>-1</sup> higher than the known median outflow velocity from the simulations, and apply this correction to our  $\Delta v$  values. This is consistent with the findings of Maltby et al. (2019).

The best-fitting Gaussians for each of our groups are shown in Fig. 3: the top panels show the fit to the full Mg II profile, while the bottom panels show the outflow component and residual flux after removal of the systemic fit. We find clear evidence for a strongly blueshifted component within the Mg II feature for our first three samples – progenitors, Quenched<sub>young</sub>, and Quenched<sub>mid</sub>. The significance of the outflow components for all three groups is  $\gg 3\sigma$ , as determined from an F-test ( $p \ll 0.05$ ). We find no evidence for any significant asymmetry within the absorption profile of our Quenched<sub>old</sub> galaxies with  $t_{\text{burst}} > 1$  Gyr, and the profile is best fit with a single Gaussian doublet, fixed at the rest-frame wavelength ( $p > 0.05$ ). The velocity offsets and corresponding  $v_{\text{out}}$  values are presented in Table 3.

Interestingly, we find that galaxies with a burst over 600 Myr ago (Quenched<sub>mid</sub>,  $v_{\text{out}} \sim 1500$  km s<sup>-1</sup>) have similarly high-velocity outflows to those with more recent bursts (Quenched<sub>young</sub>,  $v_{\text{out}} \sim 1400$  km s<sup>-1</sup>), in contrast to the findings for local galaxies (e.g. Sun et al. 2024). If these outflows originate from star formation, we would not expect them to persist at high velocities so long after the burst, and we discuss this further in Section 4.3.

Outflow velocities from the above method relies on the correct modelling of the systemic component. To explore a model-independent velocity measurement, we use a boxcar method (e.g. Rubin et al. 2010; Bordoloi et al. 2014; Maltby et al. 2019), which is useful in the case of low S/N stacks. An estimate of the mean outflow

<sup>2</sup>We direct the reader to appendix A of Maltby et al. (2019) for more detail.

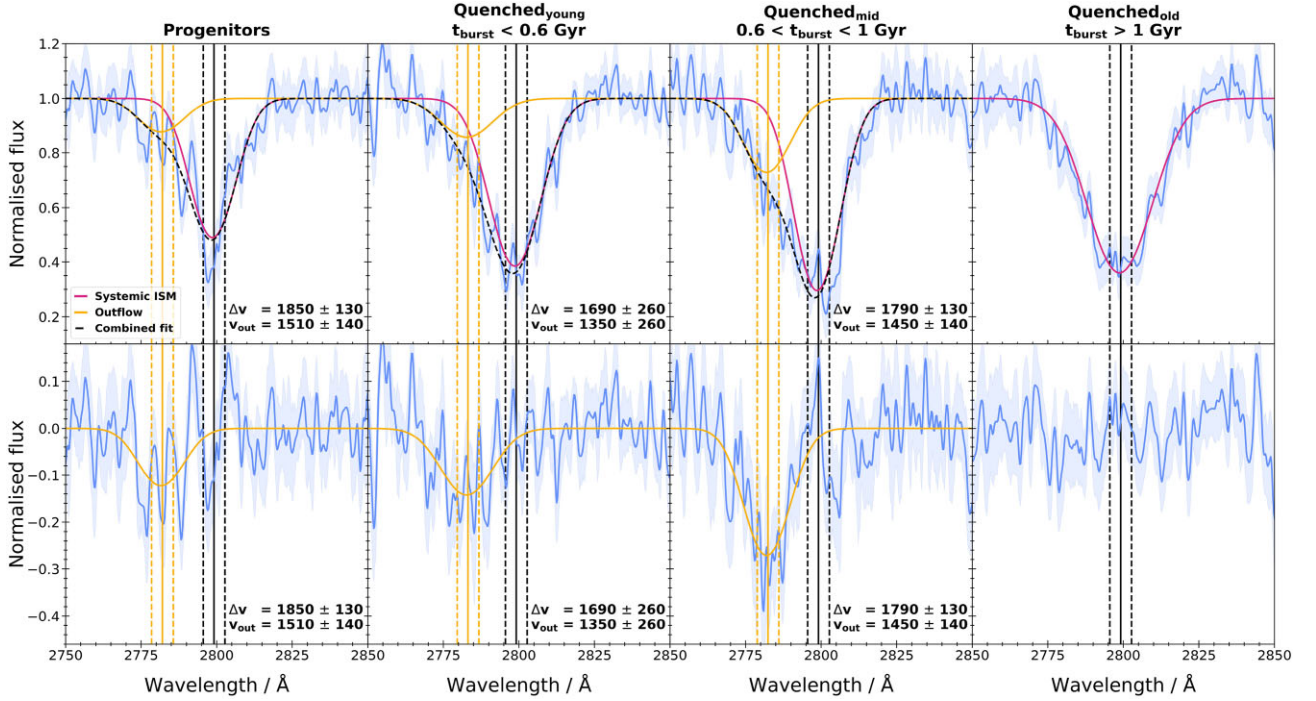


**Figure 3.** Double Gaussian model fits to the Mg II absorption feature for stacked galaxies in each of our four age samples. The spectra have been normalised and smoothed using a Gaussian filter with width  $\sigma = 1.5 \text{ \AA}$  for display purposes only. Errors in the stack (light blue shaded area) and velocity measurements are determined using 100 simulated spectra generated through a bootstrap analysis. Velocity offsets ( $\Delta v$ ) and corresponding corrected velocities after accounting for overestimations in our fitting routine ( $v_{\text{out}}$ , see Section 3.1) are in units  $\text{km s}^{-1}$ . *Top panels:* the best-fitting model to the absorption feature. The full model (black, dashed) consists of two Gaussian doublets: one fixed to the Mg II rest-frame wavelengths ( $\lambda\lambda 2796, 2803 \text{ \AA}$ , magenta), and one to model the outflowing gas component (yellow). Black and yellow vertical lines denote the rest-frame and outflow wavelengths, respectively. *Bottom panels:* the residual flux with the fitted outflow (yellow) after removal of the systemic ISM fit (magenta, top panels). We find evidence for high-velocity outflows in our progenitors ( $\Delta v \sim 1900 \pm 130 \text{ km s}^{-1}$ ) and for our Quenched<sub>young</sub> and Quenched<sub>mid</sub> ( $\Delta v \sim 1700 \pm 260$  and  $\sim 1800 \pm 130 \text{ km s}^{-1}$ , respectively). We find no evidence to suggest the outflow velocity decreases with  $t_{\text{burst}}$ , and no significant evidence for outflows in our Quenched<sub>old</sub> sample.

velocity,  $\langle v_{\text{out}} \rangle$ , can be found using

$$\langle v_{\text{out}} \rangle = \frac{W_{\text{tot}}}{W_{\text{out}}} \langle v_{\text{tot}} \rangle, \quad (1)$$

where the equivalent width of the outflow component,  $W_{\text{out}}$ , is

$$W_{\text{out}} = 2(W_{\text{blue}} - W_{\text{red}}). \quad (2)$$

Here,  $W_{\text{red}}$  and  $W_{\text{blue}}$  are the equivalent widths of the blue side ( $2775 \text{ \AA} \leq \lambda \leq 2796 \text{ \AA}$ ) and red side ( $2803 \text{ \AA} \leq \lambda \leq 2820 \text{ \AA}$ ) of the MgII feature,  $W_{\text{tot}}$  is the equivalent width of the full profile, and  $\langle v_{\text{tot}} \rangle$  is the mean absorption weighted velocity of the observed absorption line (see Rubin et al. 2010; Bordoloi et al. 2014, for full details). We determine  $\langle v_{\text{out}} \rangle$  values of  $730 \pm 110$ ,  $680 \pm 80$ , and  $760 \pm 80 \text{ km s}^{-1}$  for our progenitors, Quenched<sub>young</sub>, and Quenched<sub>mid</sub> samples, respectively (see Table 3). Our  $\langle v_{\text{out}} \rangle$  estimates are lower than those determined from the double Gaussian method, but they nevertheless show the outflows persisting through the PSB phase.

### 3.2 Double Gaussian + stellar component

In our initial simple fit, we have modelled the systemic stellar and ISM contributions to the MgII absorption feature as a single component. To determine the impact of this assumption on our results, we use full spectral fitting using synthetic stellar libraries to estimate the contribution of the stellar component to MgII.

We fit our stacks using the E-MILES stellar population synthesis models (Vazdekis et al. 2016) via the Penalized PiXel-Fitting (PPXF,

Cappellari & Emsellem 2004; Cappellari 2017, 2023) software. The E-MILES library is a theoretical set of models, covering the wavelength range  $\lambda\lambda 1680\text{--}50\,000 \text{ \AA}$  and a wide range of metallicities and temperatures. We restrict the library to models with solar metallicity, as expected for massive high- $z$  galaxies (Sommariva et al. 2012). During the fitting process, we mask the entire Mg II feature to avoid the fit accounting for all the systemic absorption within the stellar component. The fits are performed over the wavelength range  $2550\text{--}4250 \text{ \AA}$ , and then subtracted from the stacks to determine the ISM contribution to Mg II. We then fit the residual flux with a double Gaussian model as described in Section 3.1,<sup>3</sup> using the offset of the outflowing component centroid to determine  $\Delta v$ . We apply a correction to  $\Delta v$ , as outlined in Section 3.1, to determine  $v_{\text{out}}$  for each sample. We acknowledge that the E-MILES library models lack the youngest stellar populations (age  $< 30 \text{ Myr}$ ). This has no implications for our quenched galaxy populations, since these stars will no longer be present. However, the same is not true for our progenitor populations, where such stars are likely to dominate the flux output. Therefore, we repeat our fits using two additional suites of models which include such stars: GALAXEV (Bruzual & Charlot 2003) and FSPS (Conroy, Gunn & White 2009). Reassuringly, we find our results are entirely consistent, regardless of the stellar library used. The best-fitting models for each of our groups are shown in Fig. 4: the top panels show the stellar component fit using PPXF, while the

<sup>3</sup>Here, we omit step (i) from the model fitting, as removing the stellar component normalizes the absorption feature.

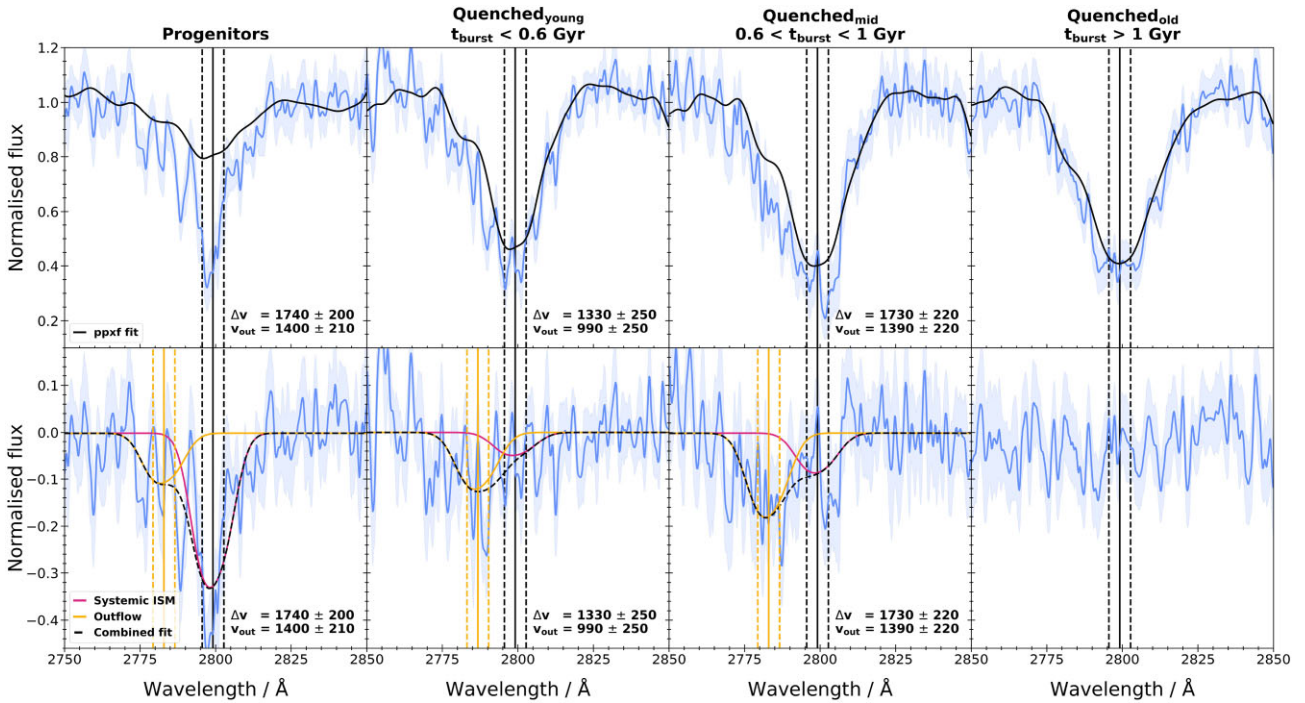


**Figure 4.** Double Gaussian + stellar model fits to the Mg II absorption feature for stacked galaxies in each of our four age samples. The spectra have been normalized and smoothed using Gaussian filter with width  $\sigma = 1.5 \text{ \AA}$  for display purposes only. Errors in the stack (light blue shaded area) and velocity measurements are determined using 100 simulated spectra generated through a bootstrap analysis. Velocity offsets ( $\Delta v$ ) and corresponding corrected velocities after accounting for overestimations in our fitting routine ( $v_{\text{out}}$ , see Section 3.1) are in units  $\text{km s}^{-1}$ . *Top panels:* the best-fitting PPDF model to the absorption feature, representing the stellar component. *Bottom panels:* the best-fitting model to the spectra once the stellar component (black, top panels) has been removed. The model consists of two Gaussian doublets: one fixed to the Mg II rest-frame wavelengths ( $\lambda\lambda 2796, 2803 \text{ \AA}$ , magenta), and one to model the outflowing gas component (yellow). Black and yellow vertical lines denote the rest-frame and outflow wavelengths, respectively. We find evidence for high-velocity outflows in our progenitors ( $\Delta v \sim 1700 \pm 200 \text{ km s}^{-1}$ ) and for our Quenched<sub>young</sub> and Quenched<sub>mid</sub> ( $\Delta v \sim 1300 \pm 250$  and  $\sim 1700 \pm 220 \text{ km s}^{-1}$ , respectively). We find no evidence to suggest the outflow velocity decreases with  $t_{\text{burst}}$ , and no significant evidence for outflows in our Quenched<sub>old</sub> sample.

bottom panels show the systemic and outflowing ISM components after removal of the PPDF fit.

We find similar velocities to our double Gaussian model using this method, and all are consistent within the errors (see Table 3). As we found when using our double Gaussian model, the significance of the outflowing components for our progenitor, Quenched<sub>young</sub>, and Quenched<sub>old</sub> samples are much greater than  $3\sigma$ , and no significant outflow component is needed to account for the profile of the Quenched<sub>old</sub> sample (see Table 3 for F-test  $p$ -values). Once again, we see the striking trend of high-velocity outflows persisting well into the PSB phase.

## 4 DISCUSSION

### 4.1 Comparison of our models

In our analysis, we use two different models to determine an estimate of  $v_{\text{out}}$  in each of our samples. Our approach in Section 3.1 was to simply fit a double Gaussian model to the overall absorption profile, which has the benefit of simplicity, and allows us to determine the significance of the outflowing component. This model could potentially be incorrect, however, if the continuum levels estimated by the spline fit are wrong. In correctly modelling the stellar component in Section 3.2, the second method ought to give a more robust results in principle, but the method is somewhat model dependent, and assumes that we fully understand and trust the stellar libraries.

Overall, our results suggest that a significant high velocity component is present in some fraction of both recently and intermediate quenched galaxies, and this seems to be robust to the method chosen. These high velocities are not necessarily the *characteristic* velocities for our samples, but the presence of such a high-velocity component is clearly important, as it will exceed the typical escape velocity of the galaxy ( $\sim 1000 \text{ km s}^{-1}$ ), and could be related to the quenching mechanism.

### 4.2 Burst ages

The supercolour  $t_{\text{burst}}$  (‘time since burst’) values used in our analysis are calculated by fitting stochastic burst models to the galaxy SEDs from the PCA analysis (see Section 2.1.1). To test the robustness of the burst age estimations, we also used the BAGPIPES code (Carnall et al. 2018, 2019) to fit the photometry and spectroscopy of our samples simultaneously, following the method of Wild et al. (2020). We refer the reader to Wild et al. (2020) for the details of the BAGPIPES star formation history modelling. We find that the  $t_{\text{burst}}$  values from BAGPIPES are strongly correlated with the ages determined from the PCA analysis, but typically  $\sim 40$  per cent older on average. Repeating the stacking analysis with the new ages, we find that our primary findings are unaffected. Significant, high velocity outflows are still observed in older quenched galaxies ( $t_{\text{burst}} > 0.6 \text{ Gyr}$ ). The only tentative difference is the persistence of outflows  $\sim 1 \text{ Gyr}$  after the burst, which we note is consistent with the older average burst ages from BAGPIPES. Very similar results are obtained using the light-

weighted ages from the PCA analysis (Wild et al. 2014), and by using alternative age estimates proposed by Belli, Newman & Ellis (2019), determined from position in a UVJ colour–colour diagram. We conclude that our primary findings are robust: high-velocity outflows are observed in relatively old, quenched galaxies, long after the starburst has ended.

### 4.3 Star formation or AGN driven winds?

At first glance, our results seem to support the scenario in which a highly SFG collapses to become extremely compact and undergoes a huge starburst, followed by rapid quenching through the removal of gas. Comparing the compactness,  $\Sigma_{1.5}$ <sup>4</sup> of our samples, we find our Quenched<sub>young</sub> and Quenched<sub>mid</sub> groups ( $\log_{10}(\Sigma_{1.5}) \sim 10.7$  and  $10.5 \text{ M}_{\odot} \text{ kpc}^{-1.5}$ , respectively) are substantially more compact than our progenitors ( $\log_{10}(\Sigma_{1.5}) \sim 9.9 \text{ M}_{\odot} \text{ kpc}^{-1.5}$ ). The difference in  $\Sigma_{1.5}$  values indicates our progenitors are likely to undergo rapid compaction either before or during the starburst. PSBs at high redshift have been found to be highly compact (e.g. Yano et al. 2016; Almaini et al. 2017; Maltby et al. 2018). Various studies at intermediate redshifts ( $z \sim 0.6$ ) have concluded that high-velocity outflows in quenching galaxies are likely driven by feedback associated with highly compact starbursts (e.g. Diamond-Stanic et al. 2012; Sell et al. 2014; Perrotta et al. 2021; Davis et al. 2023).

Locally, PSBs have been found to have decreasing wind velocity with increasing  $t_{\text{burst}}$ . Sun et al. (2024) found that outflow velocity decreases with elapsed time since an episode of bursty star-formation, for  $z < 0.3$  starbursting and PSB galaxies. If the outflows we are detecting in the Quenched<sub>young</sub> and Quenched<sub>mid</sub> groups originate from their latest period of star formation, we would not expect them to persist at high velocities long after the burst. Our Quenched<sub>young</sub> and Quenched<sub>mid</sub> galaxies have typical effective radii of  $R_e \sim 1\text{--}2 \text{ kpc}$ ; an outflowing wind with velocity  $v_{\text{out}} = 1000 \text{ km s}^{-1}$  would travel  $\sim 100 \text{ kpc}$  in 100 Myr, so on time-scales longer than this an outflow should have long cleared the galaxies in our sample if they are driven solely by star formation. A simple explanation for this could be that these winds are not fueled by star formation alone, and are driven by feedback from AGNs, as some authors suggest. For example, Tremonti et al. (2007) attribute the  $\sim 1000 \text{ km s}^{-1}$  outflows in their PSB sample at  $z \sim 0.6$  to AGN feedback based on detection of [O III] in the spectra, with equivalent width values matching those of powerful AGNs. Davies et al. (2024) also found evidence for AGN activity in galaxies with high-velocity neutral gas outflows in the redshift range  $1.7 < z < 3.5$  (see also Park et al. 2023).

Previous studies at  $z < 1$  have found some PSB galaxies to have optical emission line ratios falling within the LINER region of BPT diagrams (e.g. Wild et al. 2007; Brown et al. 2009; Wild, Heckman & Charlton 2010; Alatalo et al. 2016). Optically selected AGN fractions in PSB samples vary from  $\sim 5$  per cent (Greene et al. 2020) to  $\sim 35$  per cent (Yesuf et al. 2014), and younger PSBs have been found to have an AGN fraction a factor of 10 times higher than that of older PSBs (Greene et al. 2020). There is evidence, however, that shocks and/or post-AGB stars may cause LINER-like emission line ratios (e.g. Yan & Blanton 2012; Rich, Kewley & Dopita 2015), and PSB selection methods vary between studies. At  $z > 1$ , however, the incidence of PSBs hosting AGN is unclear.

While our  $z > 1$  Quenched<sub>young</sub> and Quenched<sub>mid</sub> stacks have outflows detected, they show no AGN signatures in the available

optical data (individually, or in the stacks). This is consistent with the findings of Maltby et al. (2016). Due to the redshift range of our data, we acknowledge that the spectra used in this work cover only a few, typically faint, high-ionization lines (e.g. [Ne V]  $\lambda 3427 \text{ \AA}$  and [Ne III]  $\lambda 3870 \text{ \AA}$ ). However, [Ne V] is commonly seen in local AGNs, and provides a useful diagnostic even at high levels of obscuration (e.g. Gilli et al. 2010). The lack of [Ne V] in our stacks would therefore suggest a lack of significant AGN activity. However, a more detailed multiwavelength analysis would be required to rule out the presence of AGN in our sample, which is beyond the scope of this work. A full analysis of the prevalence of X-ray detected AGN in recently quenched galaxies will be presented in Almaini et al. (in preparation).

The lack of evidence for active AGNs in our stacks does not necessarily imply purely star formation driven outflows: the winds may be relic outflows, launched by previous episodes of AGN activity. We may be observing these ‘fossil’ AGN outflows, which are expected to persist for several times the duration of the AGN-driven phase (Zubovas & Maskeliūnas 2023). Episodic AGN activity could persist well into the PSB phase, maintaining the outflows, but due to the short duty cycle catching the PSB in this phase is unlikely (see Lanz et al. 2022; Luo et al. 2022, for examples of low-luminosity AGNs in  $z < 0.2$  PSBs). In the local Universe ( $z < 0.05$ ), French et al. (2023) found evidence of fading AGNs in five PSBs within the Mapping Nearby Galaxies at Apache Point Observatory survey. They estimate the AGN duty cycle during the PSB phase as  $\sim 2 \times 10^5 \text{ yr}$ , and that an AGN spends  $\sim 5$  per cent of time in its ‘luminous phase’ ( $\sim 1 \times 10^4 \text{ yr}$ ). The duty cycle for more distant PSBs has not yet been estimated, although there are indications that general AGN duty cycles may be longer at higher redshifts (see Delvecchio et al. 2020).

## 5 CONCLUSIONS

In this work, we use the Mg II ( $\lambda\lambda 2796, 2803 \text{ \AA}$ ) absorption feature at  $z > 1$  to investigate how galactic-scale outflows evolve with time since the last starburst ( $t_{\text{burst}}$ ). We stack deep optical spectra from the UDSz and VANDELS surveys, and find clear evidence for high-velocity outflows within our progenitors ( $v_{\text{out}} \sim 1400 \pm 210 \text{ km s}^{-1}$ ), and galaxies with  $t_{\text{burst}} < 1 \text{ Gyr}$  ( $v_{\text{out}} \sim 990 \pm 250$  and  $\sim 1400 \pm 220 \text{ km s}^{-1}$  for galaxies with  $t_{\text{burst}} < 0.6 \text{ Gyr}$  and  $0.6 \text{ Gyr} < t_{\text{burst}} < 1 \text{ Gyr}$ , respectively). We find no evidence for outflows in our passive galaxy sample with  $t_{\text{burst}} > 1 \text{ Gyr}$ . Our sample shows no signs of AGNs in their optical spectral features, which may indicate that any AGNs in these galaxies have very short duty cycles, and were ‘off’ when these galaxies were observed. The presence of significant outflows in the older quenched galaxies ( $t_{\text{burst}} > 0.5 \text{ Gyr}$ ) is difficult to explain with starburst activity alone, and may indicate energy input from episodic AGN activity as the starburst fades.

## ACKNOWLEDGEMENTS

We thank the anonymous referee for their detailed and insightful comments which helped to improve our work. ET wishes to thank Adam Carnall for useful discussions. OA acknowledges the support of STFC grant ST/X006581/1. VW acknowledges STFC grant ST/Y00275X/1. We extend our gratitude to the staff at United Kingdom Infrared Telescope for their tireless efforts in ensuring the success of the UDS project. We also wish to recognize and acknowledge the very significant cultural role and reverence that the summit of Mauna Kea has within the indigenous Hawaiian community. We were most fortunate to have the opportunity to

<sup>4</sup>From Barro et al. (2013);  $\Sigma_{1.5} \equiv M_*/r_e^{1.5}$ . This parameter effectively removes the slope of the galaxy mass/size relation.



conduct observations from this mountain. For the purpose of open access, the authors have applied a creative commons attribution (CC BY) to any journal-accepted manuscript. This work is based in part on observations from ESO telescopes at the Paranal Observatory (programmes 180.A-0776, 094.A-0410, and 194.A-2003).

## DATA AVAILABILITY

The imaging data and spectroscopy forming the basis of this work are available from public archives, further details of which can be obtained from the UDS web page (<https://www.nottingham.ac.uk/astronomy/UDS/>). A public release of the processed data and photometric redshifts is in preparation. Details can be obtained from Omar Almaini (omar.almaini@nottingham.ac.uk). In the meantime, data will be shared on request to the corresponding author.

## REFERENCES

- Alatalo K. et al., 2016, *ApJS*, 224, 38  
 Almaini O. et al., 2017, *MNRAS*, 472, 1401  
 Barro G. et al., 2013, *ApJ*, 765, 104  
 Belli S., Newman A. B., Ellis R. S., 2019, *ApJ*, 874, 17  
 Belli S. et al., 2023, *Nature*, 630, 54  
 Bordoloi R. et al., 2014, *ApJ*, 794, 130  
 Borthakur S., Heckman T., Strickland D., Wild V., Schiminovich D., 2013, *ApJ*, 768, 18  
 Bradshaw E. J. et al., 2013, *MNRAS*, 433, 194  
 Brown M. J. I. et al., 2009, *ApJ*, 703, 150  
 Bruzual G., Charlot S., 2003, *MNRAS*, 344, 1000  
 Cappellari M., 2017, *MNRAS*, 466, 798  
 Cappellari M., 2023, *MNRAS*, 526, 3273  
 Cappellari M., Emsellem E., 2004, *PASP*, 116, 138  
 Carnall A. C., McLure R. J., Dunlop J. S., Davé R., 2018, *MNRAS*, 480, 4379  
 Carnall A. C. et al., 2019, *MNRAS*, 490, 417  
 Cielo S., Bieri R., Volonteri M., Wagner A., Dubois Y., 2018, *MNRAS*, 477, 1336  
 Cimatti A. et al., 2013, *ApJ*, 779, L13  
 Conroy C., Gunn J. E., White M., 2009, *ApJ*, 699, 486  
 Davies R. L. et al., 2024, *MNRAS*, 528, 4976  
 Davis J. D. et al., 2023, *ApJ*, 951, 105  
 Delvecchio I. et al., 2020, *ApJ*, 892, 17  
 Diamond-Stanic A. M., Moustakas J., Tremonti C. A., Coil A. L., Hickox R. C., Robaina A. R., Rudnick G. H., Sell P. H., 2012, *ApJ*, 755, L26  
 Dressler A., Gunn J. E., 1983, *ApJ*, 270, 7  
 French K. D., 2021, *PASP*, 133, 072001  
 French K. D., Earl N., Novack A. B., Pardasani B., Pillai V. R., Tripathi A., Verrico M. E., 2023, *ApJ*, 950, 153  
 Furusawa H. et al., 2008, *ApJS*, 176, 1  
 Garilli B., Fumana M., Franzetti P., Paioro L., Scodreggio M., Fèvre O. L., Paltani S., Scaramella R., 2010, *PASP*, 122, 827  
 Garilli B. et al., 2021, *A&A*, 647, A150  
 Gilli R., Vignali C., Mignoli M., Iwasawa K., Comastri A., Zamorani G., 2010, *A&A*, 519, A92  
 Greene J. E., Setton D., Bezanson R., Suess K. A., Kriek M., Spilker J. S., Goulding A. D., Feldmann R., 2020, *ApJ*, 899, L9  
 Hainline K. N., Shapley A. E., Greene J. E., Steidel C. C., 2011, *ApJ*, 733, 31  
 Heckman T. M., Best P. N., 2014, *ARA&A*, 52, 589  
 Heckman T. M., Borthakur S., 2016, *ApJ*, 822, 9  
 Heckman T. M., Alexandroff R. M., Borthakur S., Overzier R., Leitherer C., 2015, *ApJ*, 809, 147  
 Ibert O. et al., 2013, *A&A*, 556, A55  
 Jarvis M. J. et al., 2013, *MNRAS*, 428, 1281  
 Kauffmann G. et al., 2003, *MNRAS*, 341, 33  
 Kondapally R. et al., 2023, *MNRAS*, 523, 5292  
 Lanz L. et al., 2022, *ApJ*, 935, 29  
 Lawrence A. et al., 2007, *MNRAS*, 379, 1599  
 Leja J., Speagle J. S., Johnson B. D., Conroy C., van Dokkum P., Franx M., 2020, *ApJ*, 893, 111  
 Luo Y. et al., 2022, *ApJ*, 938, 63  
 Maltby D. T. et al., 2016, *MNRAS*, 459, L114  
 Maltby D. T., Almaini O., Wild V., Hatch N. A., Hartley W. G., Simpson C., Rowlands K., Socolovsky M., 2018, *MNRAS*, 480, 381  
 Maltby D. T. et al., 2019, *MNRAS*, 489, 1139  
 Man A. W. S. et al., 2021, *ApJ*, 919, 20  
 McLure R. J. et al., 2013, *MNRAS*, 428, 1088  
 McLure R. J. et al., 2018, *MNRAS*, 479, 25  
 Murray N., Ménard B., Thompson T. A., 2011, *ApJ*, 735, 66  
 Muzzin A. et al., 2013, *ApJ*, 777, 18  
 Papovich C. et al., 2018, *ApJ*, 854, 30  
 Park M. et al., 2023, *ApJ*, 953, 119  
 Perrotta S. et al., 2021, *ApJ*, 923, 275  
 Rich J. A., Kewley L. J., Dopita M. A., 2015, *ApJS*, 221, 28  
 Rowlands K. et al., 2018, *MNRAS*, 473, 1168  
 Rubin K. H. R., Weiner B. J., Koo D. C., Martin C. L., Prochaska J. X., Coil A. L., Newman J. A., 2010, *ApJ*, 719, 1503  
 Santini P. et al., 2022, *ApJ*, 940, 135  
 Sell P. H. et al., 2014, *MNRAS*, 441, 3417  
 Sommariva V., Mannucci F., Cresci G., Maiolino R., Marconi A., Nagao T., Baroni A., Grazian A., 2012, *A&A*, 539, A136  
 Steidel C. C., Sargent W. L. W., 1992, *ApJS*, 80, 1  
 Sun Y., Lee G.-H., Zabludoff A. I., French K. D., Helton J. M., Kerrison N. A., Tremonti C. A., Yang Y., 2024, *MNRAS*, 528, 5783  
 Talia M. et al., 2017, *MNRAS*, 471, 4527  
 Taylor E., Almaini O., Merrifield M., Maltby D., Wild V., Hartley W. G., Rowlands K., 2023, *MNRAS*, 522, 2297  
 Tremonti C. A., Moustakas J., Diamond-Stanic A. M., 2007, *ApJ*, 663, L77  
 Vazdekis A., Koleva M., Ricciardelli E., Röck B., Falcón-Barroso J., 2016, *MNRAS*, 463, 3409  
 Villeux S., Maiolino R., Bolatto A. D., Aalto S., 2020, *A&AR*, 28, 2  
 Weaver J. R. et al., 2023, *A&A*, 677, A184  
 Weiner B. J. et al., 2009, *ApJ*, 692, 187  
 Wild V., Kauffmann G., Heckman T., Charlot S., Lemson G., Brinchmann J., Reichard T., Pasquali A., 2007, *MNRAS*, 381, 543  
 Wild V., Heckman T., Charlot S., 2010, *MNRAS*, 405, 933  
 Wild V. et al., 2014, *MNRAS*, 440, 1880  
 Wild V., Almaini O., Dunlop J., Simpson C., Rowlands K., Bowler R., Maltby D., McLure R., 2016, *MNRAS*, 463, 832  
 Wild V. et al., 2020, *MNRAS*, 494, 529  
 Wilkinson A., Almaini O., Wild V., Maltby D., Hartley W. G., Simpson C., Rowlands K., 2021, *MNRAS*, 504, 4533  
 Yan R., Blanton M. R., 2012, *ApJ*, 747, 61  
 Yano M., Kriek M., van der Wel A., Whitaker K. E., 2016, *ApJ*, 817, L21  
 Yesuf H. M., Faber S. M., Trump J. R., Koo D. C., Fang J. J., Liu F. S., Wild V., Hayward C. C., 2014, *ApJ*, 792, 84  
 Zubovas K., Maskeliūnas G., 2023, *MNRAS*, 524, 4819

This paper has been typeset from a  $\text{\TeX}/\text{\LaTeX}$  file prepared by the author.